DESIGN CONSIDERATIONS FOR A "SOLAR MASS EJECTION IMAGER" ON A ROTATING SPACECRAFT

B.V. Jackson, H.S. Hudson, and J.D. Nichols

University of California, San Diego, La Jolla, CA 92093

R.E. Gold

Johns Hopkins University, Applied Physics Laboratory, Laurel, MD 20707

Abstract. We describe an instrument capable of imaging the time-varying features of the entire outer corona (from near the Sun to beyond 90° elongation) via the Thomson-scattered diffuse solar light. This "all sky" imager works on a spin-stabilized spacecraft, preferably in deep space. The design for such an imager, which can for example study solar mass ejections at great distances from the Sun, must deal with spurious signals from stray light, zodiacal light, and stars to surface brightness levels below 1 S10 unit. The design discussed here envisions a set of three slit apertures, feeding one-dimensional detectors through a lens system; the spacecraft rotation allows a complete sky survey during each spin of the spacecraft. Data clocked into a computer memory complete the "image" of the whole sky. We have analyzed a "median filter" approach to reducing the effects of starlight, in real time, on the statistics of the residual diffuse background. The analysis also included simulations of spacecraft nutation, spin-phase timing error, and image quality in the necessary wide-field optics.

Introduction

This paper describes an instrument capable of remotely sensing heliospheric disturbances via fluctuations in the surface brightness of the Thomson-scattered solar light from electrons in the solar corona and solar wind – the classical "K-corona." This instrument is not a coronagraph, however, and aims instead at imaging the entire heliosphere beyond elongation angles of about 20° (equivalent to about 80 $R_\odot$). Existing literature in this domain comes exclusively from the zodiacal light photometers onboard the Helios spacecraft (Leinert et al., 1981; Richter et al., 1982; Jackson, 1985). The physical processes to be studied include coronal mass ejections, coronal streamers, shock waves, in situ density fluctuations of the solar wind, comet bow shocks and tails, and other phenomena; see Jackson (1989) for a fuller description of the literature.

The design discussed here is for a spin-stabilized spacecraft in deep space, for example at the inner Lagrangian point (L1) of the Earth-Sun system; the model assumed in this description is the WIND spacecraft of the International Solar-Terrestrial Physics (ISTP) program (APL, 1987). A set of three cameras provide one-dimensional images of 60° width along a meridian of the ecliptic coordinate system; the satellite spin motion then scans each pixel of the one-dimensional imaging detector along a small circle of the sky, building up a complete image.

The imaging data in the WIND configuration needed to be compressed to ~50 bits per second, implying coarse angular pixels, onboard processing, and a slow cadence of observation. These compromises necessarily affect image quality, and one of the main purposes of our study has been to prepare for intelligent trade-off decisions in the different instrument parameters.

Description

The instrument consists of three cameras covering 60° ranges of ecliptic latitude, with field optics and detectors giving image-resolved data (128 pixels) in the latitude direction and 2.5° integration in azimuth. A clock divides the azimuth range into 2.5° sectors, or 20.8 ms time bins at a spin rate of 20 rpm. The resulting pixels are approximately 0.5° wide in latitude by 2.5° (FWHM of triangular response) in the azimuth direction. The pixels are then combined electronically into 2.5° × 2.5° "superpixels," which can be integrated in an onboard memory for accumulation periods of up to 1 hour for transmission at low rate through the telemetry. In the numerical simulations described in the next section, we have made slightly different assumptions about the superpixel and pixel geometry. These differences should not affect the general conclusions.

The three cameras view, respectively, from -90° to -30°, -30° to +30°, and +30° to +90° ecliptic latitude. Scattered light from the Sun, and to a lesser degree the Moon, presents problems for the camera at small elongations, and the camera lens and the image it forms must therefore be carefully baffled. A schematic of the camera front end is sketched in Figure 1a along with its configuration on a rotating spacecraft (Figure 1b). Following the basic principles of scattered-light control described by Leinert and Klüppelberg (1974) for the Sun-crossing baffle, we have laid out a baffle as sketched in Figure 2. We calculate that this baffle and a clean lens system can maintain a scattered light level well below that of the background sky beyond ~20° elongation. In order to avoid detector saturation, a "bright object sensor" will actuate a shutter mechanism to block the detector physically from sunlight within about 10° elongation.

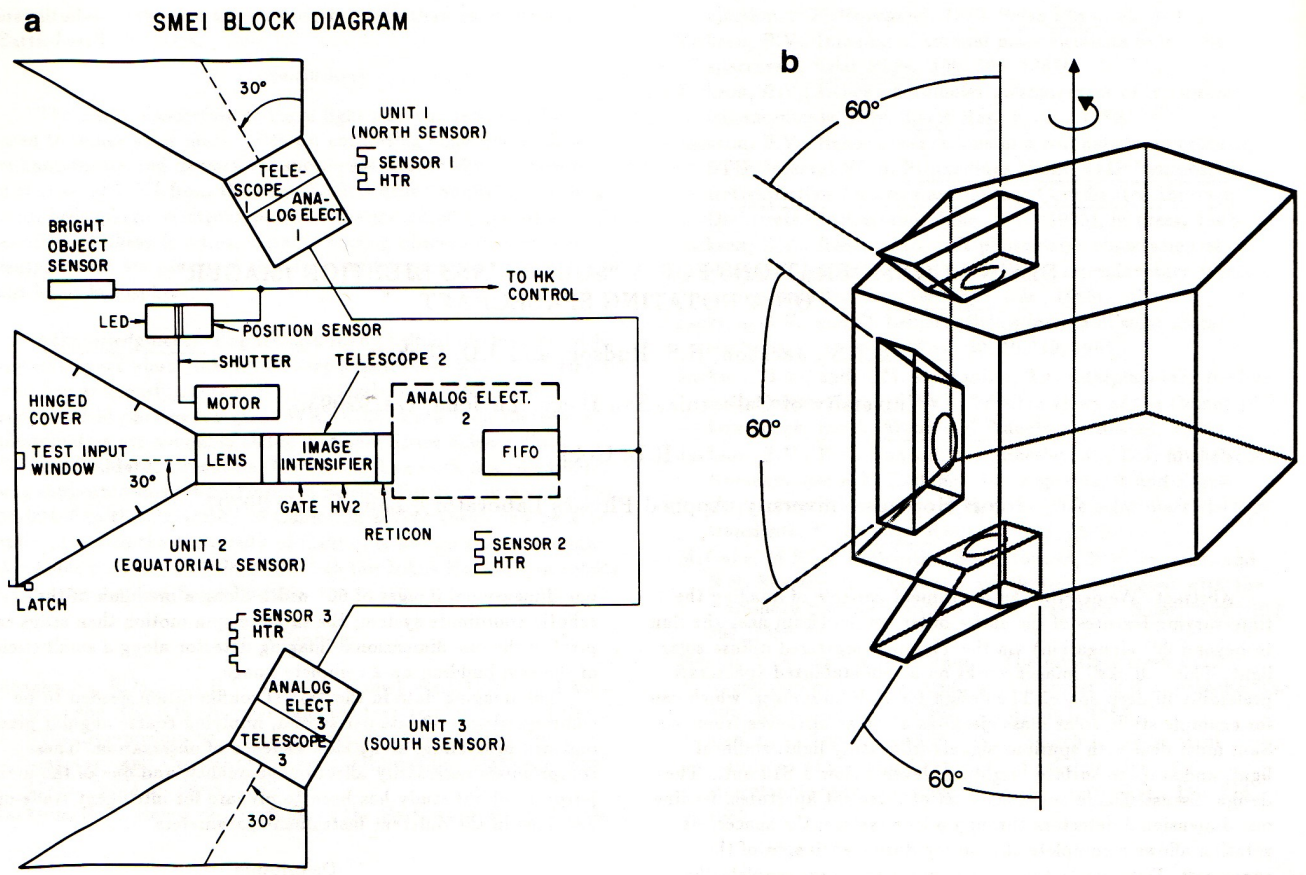

Fig. 1. Camera schematics. (a) The baffle/lens/detector system for a solar mass ejection imager designed for a rotating spacecraft. (b) As configured on a rotating spacecraft.

Signal Levels Expected

The Thomson-scattered coronal light must be detected in the presence of background diffuse light from many sources: scattered light from bright sources such as the Sun, Moon, or Earth; the zodiacal light and Gegenschein; and the stars themselves, either individually as bright point sources or collectively as a contribution to the diffuse sky brightness. The ultimate limit of diffuse-light sensitivity should be set by photon counting statistics; this limit depends upon the optics and scanning configuration, spectral bandpass, and total detector efficiency. The total detected photon count N can be approximated by

$$\log N = 4.95 - 0.4m_V + 2\log D + \log(\Delta t) \qquad (1)$$

where m_V is the stellar visual magnitude, D the aperture (diameter) in cm, and Δt the integration time in seconds; this formula assumes 10% overall quantum efficiency and 20% spectral bandwidth. Astronomical surface brightness can be expressed in "S10 units," equivalent to the flux of one, tenth-magnitude star per square degree; in these terms the background sky brightness varies roughly over the range 100-6000 S10 between the darkest sky and the ecliptic plane at solar elongations $\geq 20°$. This corresponds, according to the above formula, to photon counting rates as low as 1000 counts/s for a 1-s integration 1° pixel through 1-cm optics. This corresponds to a minimum 1-σ photometric error of ~3 S10 in a 1-s direct exposure. Across the darker areas of sky in the spin-sampling environment we expect to gather only a tiny fraction of these number of counts on any given pass. Thus, we conclude that we must count photons with our detectors, and that the signal-to-noise ratio of the instrument will be limited by integration times, viewed area of sky, and the size of the aperture when we view typical heliospheric features (see below).

Table 1 estimates the signal levels expected for various phenomena at 1 AU, on the assumption that the feature in question moves outward at constant velocity without dispersion. The brightnesses of coronal mass ejections (CME's) and streamers were derived from features traced outward from the Naval Research Laboratory (NRL) SOLWIND coronagraph to the Helios photometer field (Jackson, 1989). Shock brightnesses were estimated from the in situ plasma density enhancements behind shocks observed from the Helios spacecraft, and assumed to be viewed at 60° and 90° from the Sun-spacecraft line.

The noise estimates (Table 2) are based upon Helios photometric data taken at 0.85 ± 0.06 AU, supplemented with estimates of brightness fluctuations due to starlight. The final estimates ("all-sky") assume an all-sky imager similar to that described here, but with capability for removal of the effects of stars to different levels: seventh and ninth magnitude.

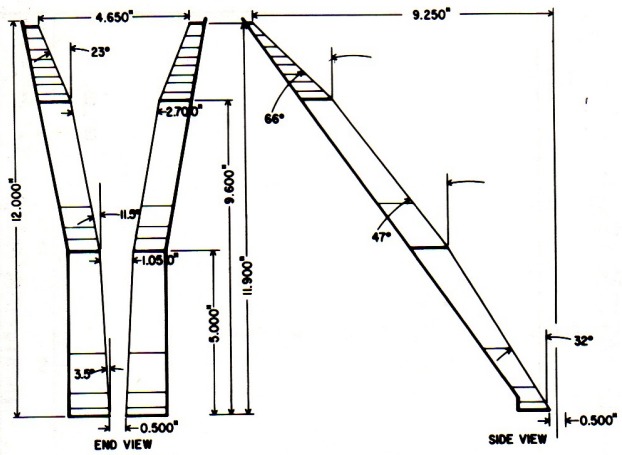

Fig. 2. Baffle layout for the Sun-crossing ecliptic baffle, showing cross-sections in the wide and narrow dimensions and the defining aperture stops. The wide dimension is oriented ecliptic NS and the spacecraft spin scans the narrow dimension, which is imaged on a one-dimensional detector, around the sky. In the narrow dimension, three "stages" of baffling can be identified by the successively narrower angles allowed to incident radiation. For this design, the volume available within the spacecraft did not permit a three-stage design in the wide dimension.

Simulations of Imaging Data

Overview

We have carried out numerical simulations of data from an imager of this design, using selected parts of the sky to provide representative background light levels. The light sources included bright stars (with $m_V \leq 10$) taken from a machine-readable version of the Smithsonian Astrophysical Observatory (SAO) sky catalogue. Diffuse light sources due to zodiacal light, the Gegenschein, and faint galactic stars were taken from tabulated values in Roach and Gordon (1973) and interpolated using a bicubic spline approximation. The actual parameters used in the simulations may differ in some details from those described above, but the results should be generally applicable. Fuller details on the numerical simulations are given by Nichols (1987).

The pixel extent was taken to be 0.5° in latitude, 2.5° in longitude. The electronics are assumed to be able to create 2.5° × 2.5° superpixels composed of five adjacent subpixels. Counts from each pixel are integrated for 1/144 of the spacecraft's 3-s spin period. This means that each pixel sweeps for 2.5°, giving each superpixel a range of 2.5° in latitude and 2.5° (FWHM) in azimuth. The range in ecliptic longitude measured increases with latitude by a factor

$$\arccos\left(\frac{\cos(2.5°)}{\cos(\beta)^2} - \tan(\beta)^2\right) \qquad (2)$$

where β is the ecliptic latitude.

A simulation run consisted of making a time series of data from a superpixel viewing a given sector of the sky. The simulated photon count rate was given by equation (1) assuming a 1-cm diameter aperture. Two time scales were relevant: the averaging time and the total measurement time. Each rotation of the spacecraft gives the sample pixel a "flash" view of the sample sky sector. These flash samples are accumulated, with appropriate statistics, over the averaging time to get the total number of counts. An accumulated image is then sent out in the telemetry stream. The total measurement time determines how many of these values are generated in the simulation. The numbers determined for each run include the average brightness of the pixel in S10 units, and the standard deviation of the sample points around that mean. The standard deviation is significant because it measures the sensitivity of the instrument; we will be unable to determine real changes below the level set by statistical fluctuations and the various sorts of uncertainties discussed below.

A number of different superpixels were used for the simulation, in order to include representative sections of the sky containing different levels of diffuse light and bright stars. Table 3 lists these trial regions, giving identification numbers and sky location (β giving the ecliptic latitude, λ the ecliptic longitude).

TABLE 1. Signal Levels Expected at 1 AU

Feature	Elongation degrees	Signal S10	Signal Duration days
Bright CME	60	3	1.5
	90	2	1.5
Bright streamer	60	2	1
	90	1	1
Bright shock	90	1-2	0.5
Major in situ	60	3	2
fluctuation	90	2	2
Comet shock	20	3-10	0.1

TABLE 2. Noise Estimates

Elongation degrees	Bandpass days	Ambient Medium* S10	Helios S + N S10	All-Sky, S10 m = 7	All-Sky, S10 m = 9
60	0.2-4	1.0	1.6	0.5-1	0.1
90	0.2-4	0.5	1.3	0.5-1	0.1

* Assumes an Allen $1/r^2$ heliosphere

TABLE 3. Pixels Used in Simulation Studies.*

Pixel No.	β	λ
1	70.0	267.6
2	50.0	269.3
3	30.0	269.8
4	10.0	270.0
5	−12.5	270.0
6	−32.5	269.8
7	−52.5	269.3
8	−72.5	267.6
11	−72.5	157.6
12	−52.5	159.3
13	−32.5	159.8
14	−12.5	160.0
15	10.0	160.0
16	30.0	159.8
17	50.0	159.3
18	70.0	157.6

*β is the ecliptic latitude and λ is the ecliptic longitude. The values given are the minimum for each 2.5° × 2.5° superpixel. Note that the apparent $\Delta\lambda$ increases at large β by the factor given in equation (2).

The effects of a number of different types of errors were simulated, including: spacecraft nutation, resulting in ecliptic latitude pointing error; timing error, resulting in errors in azimuthal binning of data; and fuzziness in the star images on the detector surface due to imperfect optics. The standard deviation of the brightness is measured for a range of these parameters. The average brightness itself (determined over the total measurement time) seems insensitive to these errors.

Underlying these simulated systematic effects is the unavoidable fluctuation due to photon counting statistics. In order to minimize this effect, most of the the simulation runs were with averaging times of 15 min of spacecraft time (or 300 rotation periods). Some of the test runs were done for 60 min of spacecraft time; Poisson statistics predicts that the fluctuations would be reduced by a factor of $\sqrt{60/15} = 2$, and this ratio was generally observed between 15- and 60-min test run simulations.

An additional feature of the simulation was a test of a "median filter" star rejection scheme, designed to remove subpixels containing bright stars from the averaging. The purpose of this procedure is to reduce the overall telemetry requirement to less than about 50 bps. The median filter scheme simply excludes the brightest 0.5° subpixels from averaging into the 2.5° superpixel sums for telemetry, thus (in principle) excluding the photon statistics due to bright stars. The median filter would be easy to implement electronically as a simple sorting of the subpixel data prior to summation. A possible defect of the median filter approach is that a bright star near a pixel boundary could cause noise-like time variations as a result of pointing errors of various types. The median filter was examined for the range of cases where we took data from only the dimmest pixel, the two dimmest pixels and so on up to all five pixels (filter disabled). The interaction of the median filter with the various errors was also considered.

Nutation Error

Simulations were run for eight pixels with four different values of nutation amplitude (A_{ν}) at an assumed period of $T_{\nu} = 20$ s. Results for other values of T_{ν} should be similar, as long as the nutation period was much shorter than the averaging time and was not an exact multiple of the spin period. The latitude pointing was assumed to be changed by an additive factor of

$$A_{\nu} \sin(2\pi t/T_{\nu}) \tag{3}$$

The sensitivity of the standard deviations of the measured brightnesses varied greatly among the pixels, as is seen in Table 4.

TABLE 4. Dependence of Sensitivity on Spacecraft Nutation Amplitude (A_{ν}) for a Fixed Star Image Radius (R_*)*

Pixel No.	R_*	$\sigma_{0\nu}$	S_{ν}
11	0.00	0.92 ± 0.01	2.95 ± 0.32
11	0.20	0.50 ± 0.11	6.02 ± 0.81
12	0.00	0.93 ± 0.22	1.87 ± 1.76
12	0.20	0.88 ± 0.04	0.57 ± 1.00
13	0.00	0.70 ± 0.10	2.56 ± 0.53
13	0.20	0.67 ± 0.05	5.10 ± 0.29
14	0.00	0.74 ± 0.10	0.58 ± 0.63
14	0.20	0.85 ± 0.16	-0.20 ± 1.06
18	0.00	0.83 ± 0.12	14.14 ± 1.03
18	0.20	0.71 ± 0.10	3.47 ± 1.12

*Values are the result of a least-squares fit to $\sigma = \sigma_{0\nu} + S_{\nu} \times A_{\nu}$.

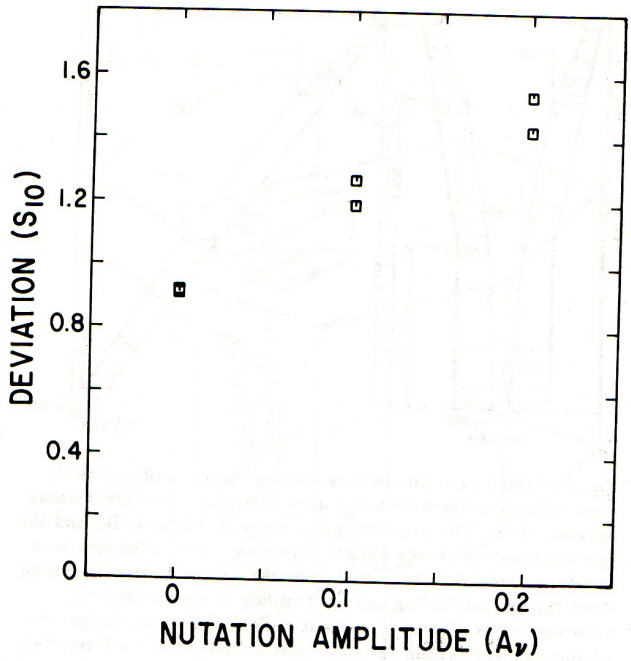

Fig. 3. Simulation results for a typical case of spacecraft nutation, showing the decrease of sensitivity (increase of scatter in S10 units) with nutation angle, as described in the text. The results of linear fits to this relationship for other pixels are given in Table 4. The results show that nutation is an important factor governing sensitivity, and that if it can be kept small enough the measurement error can be below 1 S10 unit (rms) in a 15-min integration.

Figure 3 shows the results for a typical pixel, and Figure 4 shows the worst case observed. Pixel 18 is the worst, with the measured spread increasing by a factor of 4 for a nutation magnitude of 0.2°. This case will be treated later. Linear fits were done for each pixel to the form

$$\sigma = \sigma_{0\nu} + S_{\nu} \times A_{\nu}(\text{degrees}) \tag{4}$$

Not all of the curves were linear, but the fits give an indication of the sensitivity of the spread in the brightnesses to the increase in the nutation amplitude. If pixel 18 is excluded, the average slope is 1.9 S10/deg, and all of the slopes are non-negative. As expected, increasing the latitudinal pointing error increases the value of σ. If we want to limit the deviation due to nutation to ~0.1 S10, then the nutation must be limited to ~0.05°.

The distinctive feature (at least among the pixels considered) of pixel 18 is a bright star (magnitude 4.90) near a subpixel boundary. (The star is at $\beta = 72.03°$, and the subpixel boundary is at 72.0°.) When the nutation amplitude becomes greater than 0.03°, the deviation measured jumps abruptly from about 0.6 to 2.2 S10. This suggests an explanation in terms of count truncation. The loss of one count per flash due to the fact that counts come only in integer values would give a change of 2 S10 for a subpixel, which is the correct order of magnitude.

Effects of Timing Error

Timing error would result from the Sun pulse being read inexactly, so that the azimuthal angle when a given pixel is enabled would differ slightly from one spin to the next. The effects of the

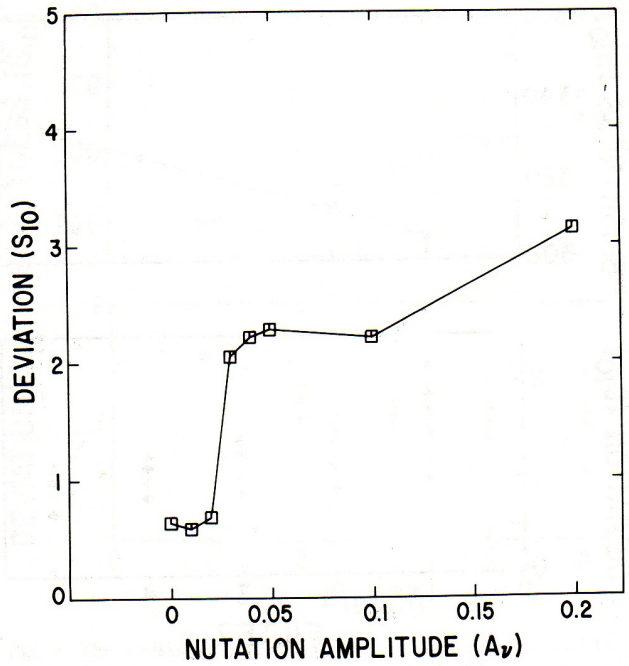

Fig. 4. Nutation results for the worst-case pixel, no. 18 in Table 1, showing that nutation-induced error can become intolerably large.

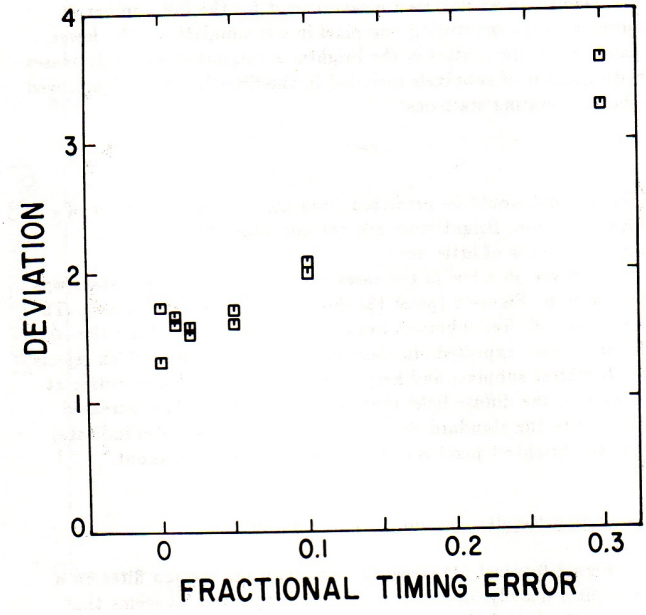

Fig. 5. Timing error results for pixel 5, showing the decrease of sensitivity (increasing scatter in S10 units) with increasing fractional timing error. This pixel was the worst in the simulation list (Table 1), and a more typical pixel did not show a significant sensitivity to timing error. See Table 5 for the simulation results of the other pixels studied.

TABLE 5. Dependence of Instrument Sensitivity on the Fractional Timing Error (ϵ).*

Pixel No.	σ_{0t}	S_t
1	0.718 ± 0.032	−0.049 ± 0.210
2	0.900 ± 0.017	0.390 ± 0.141
3	0.981 ± 0.036	−0.183 ± 0.314
4	1.127 ± 0.006	0.086 ± 0.033
5	1.491 ± 0.033	5.537 ± 0.614
6	0.981 ± 0.027	−0.021 ± 0.227
7	0.728 ± 0.007	0.531 ± 0.174
8	0.755 ± 0.004	0.264 ± 0.046

*The values are a result of a least-squares fit of $\sigma = \sigma_{0t} + S_t \times \epsilon$.

timing error were measured for eight pixels assuming perfect optical sharpness and no spacecraft nutation. The errors were considered to be normally distributed, and ranged from 0 to 30% of the flash (6.2 ms or 0.75°). The worst pixel is shown in Figure 5, and Table 5 details other results.

The results were in general analogous to those for nutation. The scatter in pixel brightness determinations is not very sensitive to errors in the initial azimuth of a pixel. The few extreme cases such as pixel 5, with a bright star near the boundary, could be masked out and disregarded in data analysis.

Optical Fuzziness

The effects of imperfection in the optics were also considered. As above, linear fits were made to

$$\sigma = \sigma_{0f} + S_f \times R_*(\text{degrees}) \tag{5}$$

for four values of R_*, the radius of an assumed disk-shaped image of uniform brightness. The selected maximum value for R_* of 0.2° meant that no star fell in more than two pixels at once. The light from a star falling in multiple subpixels was divided according to the areas of the intercepted parts of the images. Figure 6 gives the dependence of the scatter in brightness determination on optical fuzziness, for a range of nutation amplitudes, for a typical pixel. Table 6 shows the results for some of the pixels. Note that these are the same data as in Table 4, except that now A_ν is held constant and σ is considered a function of R_*. If we again exclude pixel 18 the slopes are generally small, and of mixed signs. The average slope is −0.2 S10/deg, so a decrease in optical precision actually increases the sharpness in our brightness measurement. Generally, it seems that optical precision is not that critical, which is not surprising, since only items which are point sources (e.g., stars) create a nuisance, and smearing them out should decrease their bad effects. This can be seen acting strongly in pixel 18: if $A_\nu = 0.2°$ then $\sigma = 3.6$ S10. Smearing the stars out to 0.2° radii decreases σ to ~1.2, which is nearing usability. Perhaps one could redeem a number of otherwise useless pixels by defocussing without harming the resolution on the others. We have not actually counted the pixels that would fall in this category.

The Median Filter

All of the above tests were run with the median filter engaged, so that results were obtained for five sets of filters, where the i th filter result is given by the average of the i dimmest subpixels.

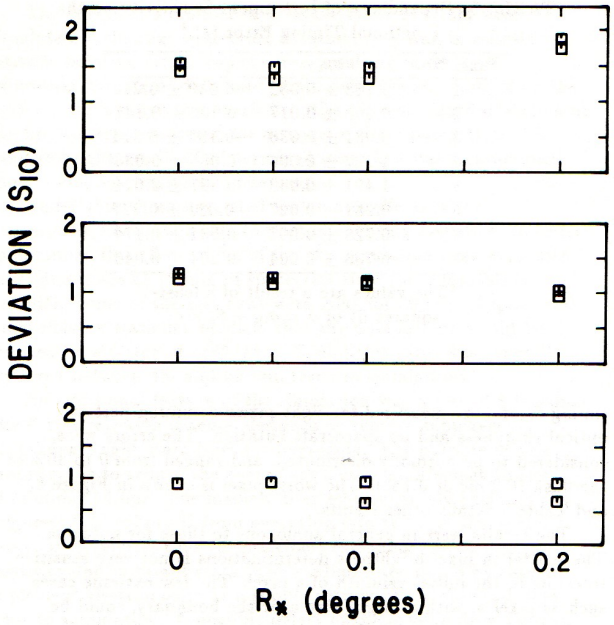

Fig. 6. Results for imperfect ("fuzzy") optics, simulated as disk-shaped stellar images of radius R_* degrees, for three different nutation amplitudes from bottom to top of 0.0°, 0.1° and 0.2° for pixel 11. See Table 6 for further results. As expected, the sensitivity does not depend strongly upon image quality, because fuzzy images reduce the contrast across the detector.

The model was run on the 18 pixels described in Table 1 and the brightness and the standard deviation of the brightness were examined as a function of filter number. Five different runs were done for each case, and the means and standard deviations of the brightness and its standard deviation were computed for each superpixel and filter.

In many of the cases the filter had no effect. Figure 7 shows a typical case (pixel 11) ; the brightness increases in a linear fashion as more subpixels are used, while the standard deviation decreases.

TABLE 6. Dependence of Sensitivity on Star Image Radius (R_*) for a Fixed Spacecraft Nutation Amplitude ($A_{n'}$).*

Pixel No.	$A_{n'}$	σ_{0*}	S_*
11	0.00	0.92 ± 0.01	-0.31 ± 0.71
11	0.20	1.40 ± 0.07	1.61 ± 0.56
12	0.00	0.87 ± 0.03	0.03 ± 0.29
12	0.20	1.29 ± 0.20	-1.49 ± 1.61
13	0.00	0.69 ± 0.06	-0.09 ± 0.46
13	0.20	1.05 ± 0.02	2.64 ± 0.19
14	0.00	0.77 ± 0.09	0.61 ± 0.98
14	0.20	0.85 ± 0.06	-0.21 ± 0.71
18	0.00	0.77 ± 0.09	-0.19 ± 0.73
18	0.20	3.37 ± 0.13	-9.91 ± 1.29

*Values are the result of a least-squares fit to $\sigma = \sigma_{0*} + S_* \times R_*$.

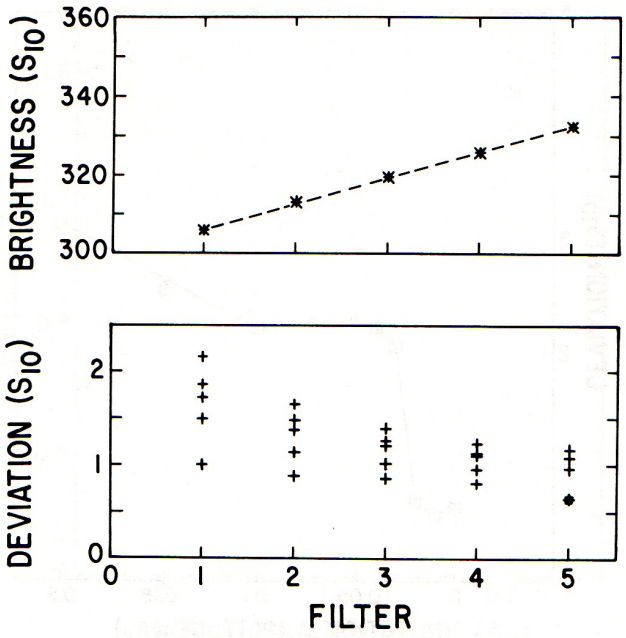

Fig. 7. The median filter at work: five simulation runs on a typical pixel, no. 11. The upper panel shows the estimated surface brightness in the pixel simulated with number of subpixels included by the median filter. As expected, the median filter biases the measurement towards low surface brightnesses. The dashed line shows the trend that would be expected for a constant-brightness sky, leading to an unbiased measurement for the full number of subpixels (5) constituting one pixel in our simulation. The lower panel shows the scatter in the brightness estimates, which decreases with number of subpixels included in the filter because of improved photon counting statistics.

This is what would be predicted from the increasing number of photon counts. Bright stars are not important here, and the median filter is of little use.

However, in a few of the cases the effect of the bright stars was clearly seen. Figure 8 (pixel 12) shows an example of this case. The case where all five subpixels are used clearly deviates from the linear relation expected. In these cases a median filter which rejects the brightest subpixel and keeps the other four is clearly better at measuring the diffuse light than a simple average. The increased variance in the standard deviation of the brightness also indicates that the brightest pixel is one that we can well do without.

Simulation Results: Instrumental Errors Included

Figure 9 (pixel 11) shows the effects of the median filter on a superpixel heavily affected by spacecraft nutation. It seems that the standard deviation of the brightness is heavily dependent upon the total number of photon counts, which means that the median filter is exactly the wrong approach to take here, since it throws away a portion of the counts. Another effect which could be operating here is that nutation, for example, could systematically change the list of subpixels selected by the median filter. Since the individual subpixels always contain intrinsically different levels of

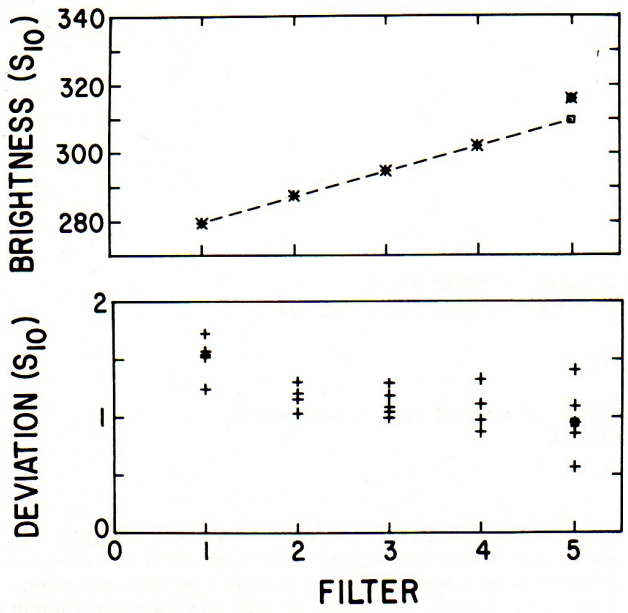

Fig. 8. The median filter at work: five simulation runs on pixel 12. This pixel contains a bright star in one subpixel. Thus, the final estimate (all five subpixels passed by the median filter) is in excess of the true value of surface brightness due to diffuse sources.

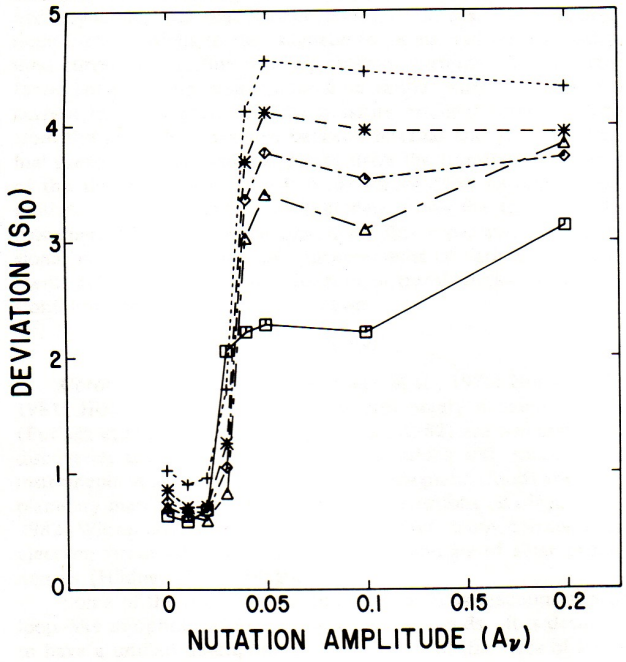

Fig. 9. The interaction of the median filter with nutation error in a case where the latter is highly significant. The + are the dimmest subpixels only, the ✳ the dimmest two subpixels, the △ three, the ◇ four, and the □ all five subpixels. This is pixel 18, to be compared with Figure 4 above.

diffuse brightness (including faint stars), the result of the median filter reselection would be to add unwanted variance. For example, when a bright star causing trouble is in a subpixel, then obviously that subpixel is not the dimmest, but when it is out, then it is the dimmest. This would definitely increase the standard deviation of the measured brightness.

Because the effects due to timing error and fuzzy star images did not seem to be much of a problem, they were not investigated in depth for their interaction with the median filter.

Conclusions

We have carried out a preliminary design for a heliospheric imager intended for a spin-stabilized spacecraft. Our analysis has shown that a rather low-resolution imager can achieve sensitivities $\geq$1 S10, if the stability of the spin motion can be maintained at a reasonable level. This is sufficiently good for studies of a number of interplanetary phenomena. We have not dealt in depth yet with scattered light problems, concentrating instead on the errors due to the background light sources and their effects on signal-to-noise ratio.

We have shown that it is possible to reject light from bright stars using an onboard algorithm (a "median filter"), allowing the data to be averaged in a meaningful way and transmitted over a narrow telemetry bandwidth. We would prefer a much higher telemetry rate than the one envisioned here, which would allow us to transmit all the data to the ground for processing. Shorter accumulation times would also allow us to study rapidly changing phenomena with time scales on the order of minutes near the Sun where there are enough photons to get accurate values. The median filter approach, although simple and in some cases effective, necessarily compromises data quality and complicates the analysis. Thus, it is to be avoided if sufficient telemetry is available to transmit all subpixel information (about 500 bps for all-sky imaging on this cadence).

Acknowledgments. The work described here was supported in part by a subcontract to the University of California at San Diego through Air Force contract F19628-87-0077 to the Johns Hopkins University Center for Applied Solar Physics.

References

Applied Physics Laboratory, All-Sky Heliospheric Imager (ASHI) Interface Control Document, JHU/APL SDO 8416, 1987 .

Jackson, B.V., Imaging of coronal mass ejections by the Helios spacecraft, Solar Phys., 100, 563, 1985.

Jackson, B.V., Heliospheric remote sensing using the zodiacal light photometers of the Helios spacecraft, these proceedings, 1989.

Leinert, C., E. Pitz, H. Link, and N. Salm, Calibration and in-flight performance of the zodiacal light experiment on Helios, Space Sci. Instrum., 5, 257, 1981.

Leinert, C. and D. Klüppelberg, Stray light suppression in optical space experiments, Applied Optics, 13, 556, 1974.

Nichols, D., Data Simulations for a Rotating Heliospheric Imager, UCSD-SP-87-23, 1987.

Richter, I., C. Leinert, and B. Planc, Search for short term variations of zodiacal light and optical detection of interplanetary plasma clouds, Astron. Astrophys., 110, 115, 1982.

Roach, F.E, and J.L. Gordon, The Light of the Night Sky, Reidel, 1973.